Dalton Transactions

ROYAL SOCIETY OF CHEMISTRY

PAPER

View Article Online
View Journal | View Issue

Cite this: *Dalton Trans.*, 2026, **55**, 1184

Multicolor luminescence of Cs_2KLuCl_6 for anti-counterfeiting and information encryption applications

Yanyang Li, Lu Lei, Sirui Shu, Jian Zou, Shanshan Hu and Jun Yang *

Received 24th August 2025,
Accepted 27th November 2025

DOI: 10.1039/d5dt02031j

rsc.li/dalton

Sb^{3+}-doped inorganic perovskites have attracted great attention for anti-counterfeiting and information encryption applications due to their excellent optical properties. We have synthesized a novel perovskite, Cs_2KLuCl_6, which exhibits weak cyan emission originating from the self-trapped excitons (STEs) of the host. Its photoluminescence quantum yield is enhanced from 2% to 68% by Sb^{3+} doping. The energy transfer channel from the STEs to Ho^{3+} was constructed, and the luminescent color was modulated from cyan to white with increasing Ho^{3+} doping concentration. The Sb^{3+}/Ho^{3+} co-doped sample has two-color luminescence performance due to the introduction of new emission centers. Up-conversion green emission was obtained by introducing Yb^{3+}/Er^{3+}. Finally, the optical properties of the obtained samples were utilized to design an anti-counterfeit label and information encryption strategy.

1. Introduction

The proliferation of counterfeiting is seriously jeopardizing socio-economic development, so the development of anti-counterfeiting and encryption technologies plays a crucial role in maintaining national economic security.[1–4] In recent decades, many anti-counterfeiting and encryption techniques have been developed, such as color patterns, bar codes and digital watermarks. However, these traditional anti-counterfeiting technologies are easily replicated and have insufficient anti-counterfeiting capabilities, so there is an urgent need to develop reliable anti-counterfeiting techniques to curb the proliferation of counterfeiting problems.[5,6] Luminescent materials activated under specific conditions are widely used in the field of anti-counterfeiting due to their advantages of flexible design, simple operation and high confidentiality,[7–9] for example, recognizing the difference between genuine and counterfeit banknotes under the irradiation of ultraviolet (UV) light. To date, many types of luminescent materials, such as metal halides,[10,11] quantum dots,[12] organic dyes[13,14] and rare-earth ion-doped materials,[15] have been developed. Among them, rare-earth elements have abundant electronic energy levels, and luminescence ranges from the ultraviolet to the infrared, showing excellent anti-counterfeiting properties.[4,16] However, an unavoidable disadvantage is the weak absorption cross-section of rare-earth ions, resulting in weak luminescence intensity. In addition, the luminescent color of materials is usually the characteristic emission of rare-earth elements, which can be easily replicated by using materials emitting the same color, so the anti-counterfeiting performance can be greatly compromised.

Lead halide perovskites have become one of the most popular materials in the field of luminescence in recent years, and have demonstrated great potential for application in the field of anti-counterfeiting and information encryption.[17–19] For example, Chen *et al.* found that the luminescent color of $CsPbBr_3$ PNCs-dichloromethane gradually blue-shifted with the extension of UV treatment time, and uniquely, the color gradually recovered after water treatment, which was attributed to the differing migration behavior of the halide ions (Cl^- and Br^-) in light and humid environments. Based on this dynamic luminescence process, which is difficult to imitate, an advanced anti-counterfeiting system has been designed.[20] However, the toxicity of lead has severely limited the commercialization of lead halide perovskites. Therefore, as next-generation materials to replace lead-based perovskites, double perovskites (DPs) have been attracting great attention in the scientific community.[21–23] In addition, since a wide variety of rare-earth ions can occupy the trivalent metal sites of DPs, more novel anti-counterfeiting materials are destined to be produced. For example, Wang *et al.* developed a novel rare-earth-based DP $Cs_2NaHoCl_6$ with enhanced down-conversion (DC) and up-conversion (UC) luminescence by Sb^{3+} and Yb^{3+} doping, respectively. Surprisingly, its UC luminescence produces changes visible to the naked eye with the increase of Yb^{3+} doping concentration or excitation power. Finally, they verified the advanced anti-counterfeiting properties of the Sb^{3+}/Yb^{3+}-doped samples.[24] Zhu *et al.* introduced Er^{3+} into

School of Chemistry and Chemical Engineering, Southwest University, No. 2, Tiansheng Road, Beibei District, Chongqing 400715, China.
E-mail: jyang@swu.edu.cn

$Cs_2NaYbCl_6$, which exhibited effective DC red emission under 380 nm excitation. Moreover, excellent UC yellow and green emission colors were exhibited under 980 and 1540 nm excitation, respectively. Finally, high-level anti-counterfeiting and information encryption applications were realized based on dual-mode multicolor fluorescence.[25]

In this paper, a novel rare-earth-based perovskite Cs_2KLuCl_6 (CKLC) was synthesized by a simple solvothermal method. Furthermore, Sb^{3+}, Sb^{3+}/Ho^{3+} and Er^{3+}/Yb^{3+} were introduced. The photoluminescence (PL) intensity from the self-trapped excitons (STEs) of the host was greatly enhanced by doping of Sb^{3+}, and the photoluminescence quantum yield (PLQY) was increased from 2% to 68%. Subsequently, the energy transfer (ET) channel of STEs → Ho^{3+} was constructed to break the weak absorption of Ho^{3+} while modulating the luminescent color. CKLC:0.3%Sb^{3+}/25%Ho^{3+} emits warm white light under UV excitation and red light under 450 nm irradiation. Using its two-color luminescence, an anti-counterfeit label was prepared. To achieve more luminescence possibilities, we also introduced Yb^{3+}/Er^{3+}, confirming its UC luminescence mechanism as a three-photon process. Finally, the obtained samples above were used together for the application of information encryption.

2. Experimental section

2.1 Chemicals

All rare earth oxides (Lu_2O_3, Ho_2O_3, Er_2O_3 and Yb_2O_3, 99.99%), KCl (99.5%), HCl (37%) and CH_3CH_2OH (99.7%) were purchased from China Chuandong Chemical Reagents Company. CsCl (99.9%, Aladdin) and $SbCl_3$ (99%, Macklin) were also used for materials synthesis in this work. To form a 0.1 mol L^{-1} $SbCl_3$ solution, 1.1406 g of $SbCl_3$ solid was dissolved in 50 mL of 12 M HCl. All chemicals were used without further purification.

2.2 Synthesis

For the preparation of pristine and ion-doped Cs_2KLuCl_6 crystals, 1 mmol CsCl, 0.4 mmol KCl and 0.25 mmol Lu_2O_3 were thoroughly ground and mixed, then loaded into a 30 mL Teflon liner, followed by the addition of 0.6 mL of 12 M HCl. $SbCl_3$ solution, Ho_2O_3, Er_2O_3 and Yb_2O_3 (while maintaining the total amount of M^{3+} as 0.5 mmol without change) were added into the above solution or solid to obtain Sb^{3+}-doped, Sb^{3+}/Ho^{3+} co-doped and Er^{3+}/Yb^{3+} co-doped Cs_2KLuCl_6 crystals. The solution mixture was heated at 180 °C for 5 h in a stainless steel Parr autoclave and then it was cooled naturally to room temperature. The products were filtered out, washed with ethanol several times and dried at 70 °C. Samples were ground into powder from crystal particles for subsequent measurements.

2.3 Characterization

The phase and structure of samples were analyzed by powder X-ray diffraction performed on a Purkinje General Instrument MSAL-XD3 using Cu Kα radiation (λ = 0.15406 nm) under the voltage and current conditions of 36 kV and 20 mA, and at a scanning rate of 8° min^{-1} in the 2θ range from 5° to 50°. The scanning electron microscopy (SEM) imaging, and the energy dispersive spectroscopy (EDS) and element mappings of the samples were conducted using a field emission scanning electron microscope (Sigma 360, ZEISS). The Raman spectra were collected on a Raman spectrometer (inVia 10400, Renishaw, UK) at 532 nm excitation. The PL, photoluminescence excitation (PLE) and time-resolved PL spectra were recorded using an Edinburgh FS5 fluorescence spectrophotometer. UC emission spectra were recorded using an Edinburgh FS5 fluorescence spectrometer combined with a 980 nm laser. PLQY measurement was carried out using an absolute PL quantum yield spectrometer (FLS1000). All characterization studies and identifications were performed at room temperature.

3. Results and discussion

3.1 Phase structure

A solvothermal method was used to obtain the CKLC DP matrix and the corresponding ion-doped samples. The crystal adopts a cubic structure belonging to the space group $Fm\bar{3}m$. Furthermore, the structure of CKLC is shown in Fig. 1a, in which K^+ and Lu^{3+} form $[KCl_6]^{5-}$ and $[LuCl_6]^{3-}$ octahedra with six Cl^-, respectively. These octahedra are arranged alternately, and Cs^+ ions with larger radius are embedded in the octahedral void. The SEM image illustrates the formation of micron-sized particles, while the element mappings demonstrate that the sample consists of the elements Cs, K, Lu, and Cl, which are uniformly distributed in the crystal (Fig. 1b). Due to having the same valence state, coordination number (CN = 6) and similar ionic radius value as Lu^{3+}, the introduced Sb^{3+}, Ho^{3+}, Er^{3+} and Yb^{3+} will occupy the lattice sites of Lu^{3+}. Powder X-ray diffraction (PXRD) patterns show that the synthesized samples match the simulated values and do not feature impurity peaks (Fig. 1c). The peak shift observed in the experimental PXRD pattern of the CKLC matrix, compared to the simulated data, can be attributed to multiple factors, including differences in the instrument, tablet thickness and doping conditions. Importantly, this systematic deviation does not affect the sample's purity. Furthermore, compared to the Cs_2KLuCl_6 matrix materials, the diffraction peaks shift toward lower angle with increasing concentration of Ho^{3+}, Er^{3+} and Yb^{3+}, suggesting expansion of the crystal lattice, which confirms the successful incorporation of dopants into the Lu^{3+} site based on Bragg's law. It is noteworthy that the diffraction peaks of Cs_2KLuCl_6:Sb^{3+} hardly shift due to the low doping concentration of Sb^{3+}. In addition, the SEM images, the element mapping results (Fig. S1–S3) and the EDS results (Table S1) of the ion-doped CKLC confirmed the material's particle size, chemical composition and homogeneous distribution of elements within the crystal. Specifically, the actual doping level is close to the nominal doping level (Table S2). Additionally, the Raman spectra (Fig. S4) of CKLC and

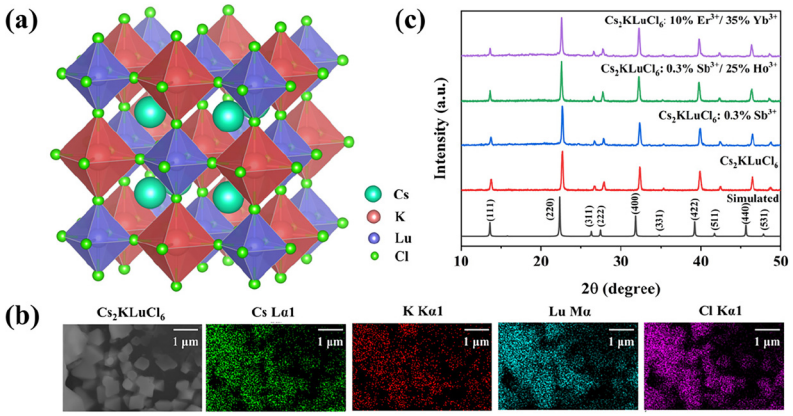

Fig. 1 (a) Crystal structure of the CKLC. (b) SEM image and element mappings of Cs, K, Lu and Cl elements in the CKLC crystal. (c) PXRD patterns of the undoped and ion-doped CKLC.

CKLC:0.3%Sb^{3+} exhibit characteristic peaks similar to those of materials such as $Cs_2NaHoCl_6$ [24] and $Cs_2NaInCl_6$.[26,27] These peaks originate from the vibrations of the $[LuCl_6]^{3-}$ octahedra, indicating the formation of a double perovskite structure.

3.2 Optical properties of Cs_2KLuCl_6 and Cs_2KLuCl_6:Sb^{3+}

We found the CKLC DP could emit faint light under UV irradiation. The PL spectrum indicates the host exhibits a broadband weak emission peaking at 498 nm with a large Stokes shift of 183 nm under 315 nm excitation (Fig. 2a). Furthermore, the PLE spectra monitored at different emission wavelengths have almost the same shape and features, proving the emission comes from the same excited state relaxation (Fig. 2b). To further study the origin of the PL emission of CKLC, we measured the time-resolved PL spectrum at room temperature. The emission at 498 nm displays slow decay with a long lifetime of 2.71 μs, excluding free exciton emission because its lifetime is generally on the ns scale (Fig. S5).[28] Therefore, we reasonably attribute the broadband weak emission with a large Stokes shift and long PL lifetime to the intrinsic host STEs of CKLC.[29,30]

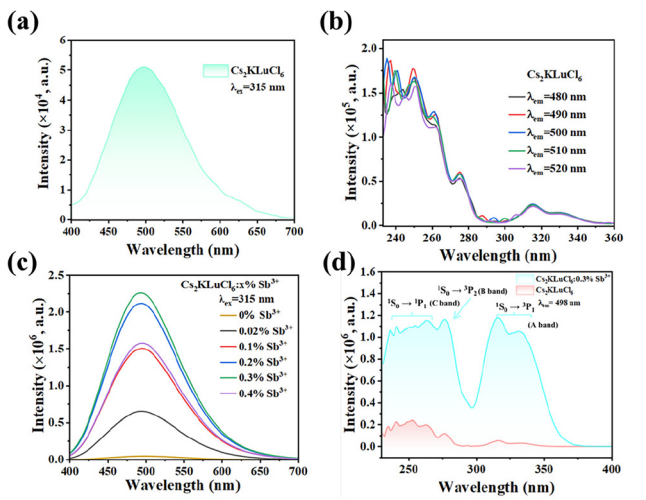

Fig. 2 (a) PL spectrum and (b) PLE spectra, monitored at different wavelengths, of CKLC. (c) PL spectra of CKLC with different Sb^{3+} concentrations under 315 nm excitation. (d) PLE spectra of CKLC and CKLC:0.3%Sb^{3+}.

Sb^{3+} with ns^2 lone pairs is commonly used as a less toxic and highly efficient dopant to form $[SbCl_6]^{3-}$ octahedra to enhance the STE emission of DPs, thus its introduction in this study.[31,32] As expected, the luminescence intensity of CKLC can be greatly increased by introducing trace amounts of Sb^{3+} due to the increased density of self-trapped exciton states and CKLC:Sb^{3+} exhibits the same PL spectra as CKLC under 315 nm excitation (Fig. 2c).[26,27,33] The luminescence intensity of CKLC is maximized when the Sb^{3+} doping concentration is 0.3 mol%, and PLQY increases from 2% in CKLC to 68% in CKLC:0.3%Sb^{3+}. The CKLC:0.3%Sb^{3+} perovskite demonstrates enhanced PLQY compared to PLQY values reported for $CsCu_2I_3$ (17.7%),[34] Cs_2ZrCl_6 nanocrystals (75.6%),[35] and $CsPbBr_3$ quantum dots (41.9%).[36] Subsequently, however, the PL intensity decreases when further increasing the Sb^{3+} concentration due to the concentration quenching effect (Fig. 2c).[37] The PLE spectra of CKLC and CKLC:Sb^{3+} further suggest Sb^{3+} doping can prompt the sensitization of STE states (Fig. 2d). In addition, the $^1S_0 \rightarrow {}^3P_1$ (A band) transition of Sb^{3+}, which has broad excitation bands with two peaks at 316 and 335 nm, may be identified. The Sb^{3+} excitation bands at about 277 nm and 250 nm can be assigned to the vibration-induced $^1S_0 \rightarrow {}^3P_2$ (B band) and dipole-allowed $^1S_0 \rightarrow {}^1P_1$ (C band) transitions, respectively.[38]

3.3 Optical properties of Cs_2KLuCl_6:Sb^{3+}/Ho^{3+}

It is well known that an effective ET channel can break the low luminous intensity caused by the small absorption cross-section of rare-earth ions.[39] Considering that CKLC:0.3%Sb^{3+} has a large excitation band in the UV region and cyan is the complementary color of red, here we introduce Ho^{3+} to modulate the luminescent color and increase its luminescence intensity. As shown in Fig. 3a, when Ho^{3+} was introduced, the

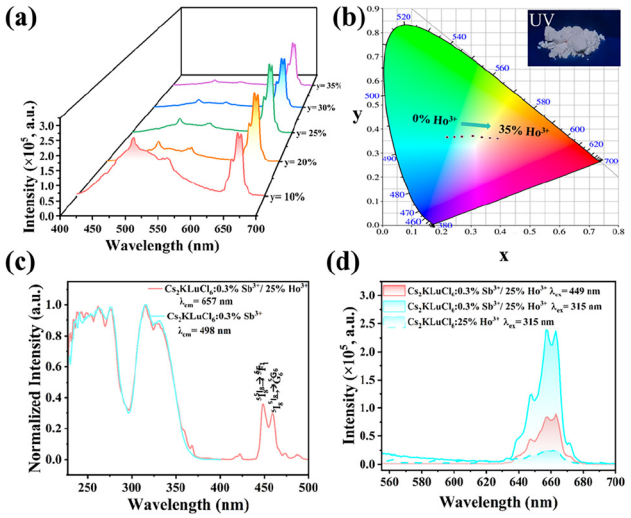

Fig. 3 (a) PL spectra and (b) CIE color coordinates of CKLC:0.3%Sb^{3+}/*y*%Ho^{3+}. (c) PLE spectra of CKLC:0.3%Sb^{3+} and CKLC:0.3%Sb^{3+}/25%Ho^{3+}. (d) PL spectra of CKLC:*x*%Sb^{3+}/25%Ho^{3+}.

characteristic emission originating from Ho^{3+} was observed in addition to STE emission under 315 nm excitation. The spectral peaks at 490, 543 and 657 nm are attributed to the $^5F_3$, $^5F_4/^5S_2$, $^5F_5 \rightarrow {}^5I_8$ transitions of Ho^{3+}, respectively. As expected, the emission of STEs originating from $[SbCl_6]^{3-}$ octahedra decreases continuously with increasing Ho^{3+} content, which is caused by the ET from STEs to Ho^{3+}, and interestingly the luminescent color also changes from cyan, first to white, and finally to red (Fig. 3b). Moreover, CKLC:0.3%Sb^{3+}/25%Ho^{3+} emits warm white light with a color coordinate of (x = 0.3377, y = 0.3672) under the excitation of 315 nm. The inset in Fig. 3b is a picture of this perovskite under UV irradiation. Unlike our previously reported Sb^{3+}/Ho^{3+} co-doped $Cs_2NaGdCl_6$,[40] in which the luminescent color can only be tuned from blue to red with increasing Ho^{3+} content. Meanwhile, the ET efficiency (η_{ET}) of CKLC:0.3%Sb^{3+}/*y*Ho^{3+} can be obtained from the following equation:

$$\eta_{ET} = 1 - \frac{\tau_s}{\tau_0}$$

where τ_s and τ_0 are the lifetime values of STEs with or without the presence of Ho^{3+}, respectively. As depicted in Fig. S6, the PL lifetime of STEs decreases with increasing Ho^{3+} content, which is consistent with the decreasing PL intensity of STEs.

The PLE spectrum of CKLC:0.3%Sb^{3+}/25%Ho^{3+} was recorded to further study the mechanism of excitation. In addition to the excitation band of STEs (230–350 nm), characteristic excitation peaks of Ho^{3+} at 449 and 459 nm are observed under monitoring of 657 nm irradiation, which correspond to the $^5I_8 \rightarrow {}^5F_1$ and $^5I_8 \rightarrow {}^5G_6$ transitions, respectively (Fig. 3c). This suggests that Ho^{3+} can be excited indirectly and directly.[41] These sharp excitation peaks are due to the f–f transitions of Ho^{3+} from the ground state to excited state. However, the excitation band at 315 nm is larger and broader than that at 449 nm and 459 nm, indicating indirect excitation of Ho^{3+} is more effective than direct excitation. A comparison of the PL spectra of CKLC:0.3%Sb^{3+}/25%Ho^{3+} under excitation at 315 nm and 449 nm is given in Fig. 3d, further illustrating that the weak absorption cross-section of the f–f transition from Ho^{3+} can be overcome by ET, thus increasing the PL intensity of Ho^{3+}. Notably, the luminescence intensity of CKLC:0.3%Sb^{3+}/25%Ho^{3+} was much greater than that of CKLC:25%Ho^{3+} under 315 nm excitation, indicating the ET channel of dopant STEs to Ho^{3+} is far more effective than the ET channel of host STEs to Ho^{3+} (Fig. 3d).

Based on the above discussion, we depict the possible mechanism of ET and transitions of CKLC:Sb^{3+}/Ho^{3+} in Fig. 4. Under UV light excitation, the electrons of CKLC:Sb^{3+}/Ho^{3+} are excited to the conduction band of the CKLC host and the 5p state of Sb^{3+}. Subsequently, due to the strong electron–phonon coupling, the excited state electrons are trapped in the $[LuCl_6]^{3-}$ and $[SbCl_6]^{3-}$ octahedra, respectively, thus forming STE emission. At the same time, due to the existence of an energy transfer channel between STEs and Ho^{3+}, part of the absorbed energy is transferred to the excited state of Ho^{3+} by radiative or non-radiative mechanisms, followed by non-radiative relaxation to ^5F_J (J = 3, 4, 5), and finally the characteristic emissions from Ho^{3+} are generated when returning to the ground state. Thus, double emissions are generated in this process and the corresponding luminescent color can be modulated by controlling the doping concentration of Ho^{3+}. In addition, the electrons in the $^5I_8$ ground state of Ho^{3+} can be directly excited to the $^5F_1$ level. After non-radiative relaxation to the $^5F_3$, $^5F_4/^5S_2$, and $^5F_5$ levels, the electrons can return to the ground state, while fluorescing blue, green, and red emission colors, respectively.

3.4 Up-conversion luminescence properties of $Cs_2KLuCl_6:Yb^{3+}/Er^{3+}$

In order to obtain more luminescence possibilities in this matrix, we continued to incorporate Er^{3+}/Yb^{3+} ions into CKLC. Because the concentration of doped ions will affect the emission intensity of fluorescent materials, it is necessary to explore the optimal doping concentration of Er^{3+} and Yb^{3+},

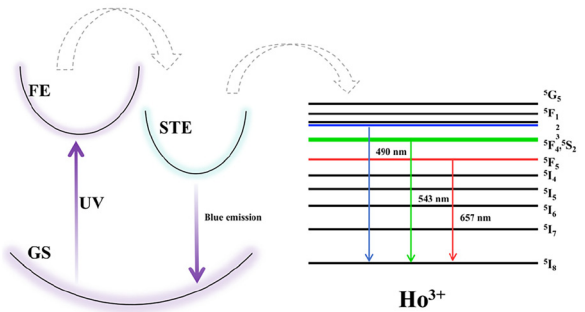

Fig. 4 Energy transfer and transition mechanism of CKLC:0.3%Sb^{3+}/25%Ho^{3+}. GS represents the ground state and FE is the free exciton state.

respectively. When fixing the concentration of Yb^{3+}, the emission position is unchanged when the doping concentration of Er^{3+} is changed, and the emission peaks consist of strong green emission ($^2H_{11/2} \rightarrow {}^4I_{15/2}$, $^4S_{3/2} \rightarrow {}^4I_{15/2}$) colors and a weak red emission ($^4F_{9/2} \rightarrow {}^4I_{15/2}$) color (Fig. 5a). The maximum intensity is reached at 10% Er^{3+} doping and then decreases due to a concentration quenching effect. Following the same method and fixing the Er^{3+} concentration, the optimum doping concentration of Yb^{3+} was determined to be 35% (Fig. 5b). The UC spectra were recorded for different pump powers to study the mechanism of UC PL. As shown in Fig. 5c, the PL intensity increases with increasing excitation power, based on the formula:

$$I \propto P^n$$

where I is the UC PL intensity at different excitation powers, P is the pump power and n is the number of photons that need to be absorbed. Thus, a plot of logarithm of I *versus* logarithm of P should yield a straight line with slope n. As presented in Fig. 5d, the slopes of UC emission are 3.02, 2.95 and 3.39 for excitation at 524, 557 and 660 nm, respectively. The values are all close to 3, suggesting that a three-photon absorption process is responsible for the green and red emission colors. Notably, the red-to-green fluorescence ratio (R/G ratio) gradually increases as the excitation power increases, and the color coordinate also changes from the green (A: 93 mW) to the yellow light region (B: 978 mW) (Fig. S7).

In general, the UC emission proceeds through a variety of processes such as ground state absorption (GSA), excited state absorption (ESA), ET and cross-relaxation (CR),[42] because the absorption cross-section of Yb^{3+} is much larger than that of Er^{3+}, and the energy absorbed by Yb^{3+} can be transferred to Er^{3+}.[43] Therefore, Yb^{3+} acts as a sensitizer for absorbing the

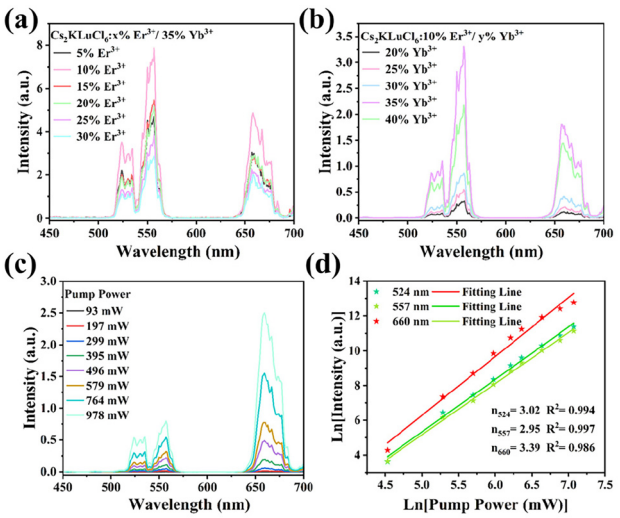

Fig. 5 (a) UC PL spectra of CKLC:x%Er^{3+}/35%Yb^{3+}. (b) UC PL spectra of CKLC:10%Er^{3+}/y%Yb^{3+}. (c) UC PL spectra with different excitation power density values and (d) the dependence of pump power as well as UC PL intensity of CKLC:10%Er^{3+}/35%Yb^{3+}.

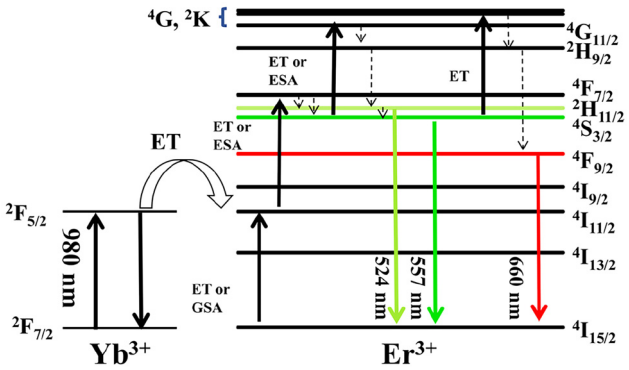

Fig. 6 UC energy transfer and transition mechanism diagram of CKLC:10%Er^{3+}/35%Yb^{3+}.

980 nm laser and Er^{3+} acts as an activator. The possible up-conversion emission schematic is depicted in Fig. 6.[44–46] After a 980 nm photon is absorbed through the GSA process, an electron of Yb^{3+} transfers from the ground state $^2F_{7/2}$ to the excited state $^2F_{5/2}$. In addition, a small number of electrons from Er^{3+} can also be excited from $^4I_{15/2}$ to $^4I_{11/2}$ through the GSA process, while most electrons of Er^{3+} are transferred to the level of $^4I_{11/2}$ by the ET of $^2F_{5/2}(Yb^{3+}) + {}^4I_{15/2}(Er^{3+}) \rightarrow {}^2F_{7/2}(Yb^{3+}) + {}^4I_{11/2}(Er^{3+})$. For the green emission, the populated $^4I_{11/2}$ level is excited to the $^4F_{7/2}$ level though the continuous ET or ESA of a second 980 nm photon. Subsequently, through non-radiation, the populated $^4F_{7/2}$ level immediately decays to the lower $^2H_{11/2}$ and $^4S_{3/2}$ levels due to the small energy gap between them, and then is excited to $^4G_{11/2}$ by the sequential ET or ESA of a third photon. Finally, the populated $^4G_{11/2}$ level is non-radially relaxed to the lower $^2H_{11/2}$ and $^4S_{3/2}$ levels. Er^{3+} will produce green emission colors at 524 nm and 557 nm by the radiative transitions from the $^2H_{11/2}$ and $^4S_{3/2}$ levels to the ground state $^4I_{15/2}$. After two-photon absorption and a series of non-radiative relaxations to the green-light emitting state ($^2H_{11/2}$, $^4S_{3/2}$), Er^{3+} continues to absorb the energy of a third photon from Yb^{3+}, sometimes transferring to a very dense variety of states labeled $^4G/^2K$. Subsequently, Er^{3+} relaxes within the $^4G/^2K$ manifold, and transfers to the level of $^4F_{9/2}$ by back energy transfer (BET) to Yb^{3+} of $^4G/^2K(Er^{3+}) + {}^2F_{7/2}(Yb^{3+}) \rightarrow {}^4F_{9/2}(Er^{3+}) + {}^2F_{5/2}(Yb^{3+})$. When electrons in the $^4F_{9/2}$ level return to the ground state $^4I_{15/2}$, red light emission is produced at 660 nm.[47]

3.5 Anti-counterfeiting and information encryption application

Due to the ET from STEs to Ho^{3+}, it can be inferred from the excitation spectrum in Fig. 3c that CKLC:0.3%Sb^{3+}/25%Ho^{3+} emits warm white light under a wide range of excitation wavelengths in the UV region (240–350 nm). As a verification process, the emission spectra of the sample were recorded at four wavelengths (Fig. 7a). At 450 nm excitation, red light is emitted due to the direct excitation of Ho^{3+}. Since two-color luminescence was obtained in a single sample, we filled the "SWU" mold with CKLC:0.3%Sb^{3+}/25%Ho^{3+}. By simply chan-

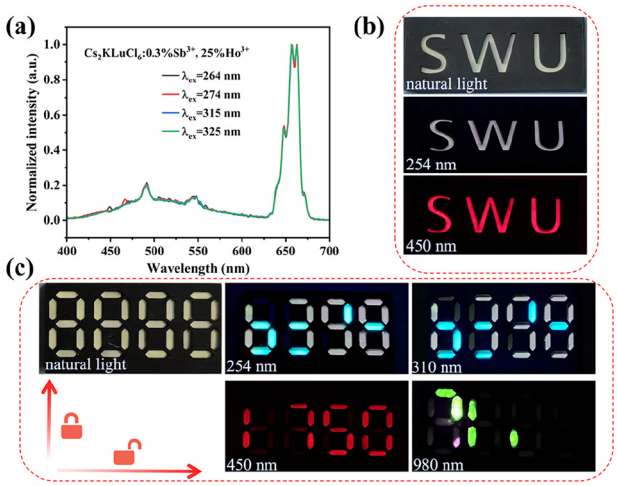

Fig. 7 (a) PL spectra and (b) digital photographs of CKLC:0.3%Sb^{3+}/25% Ho^{3+} under different excitation wavelengths. (c) Digital pictures of digital molds coated with CKLC samples under different excitation wavelengths.

ging excitation wavelengths, the objective of two-color anti-counterfeiting can be achieved (Fig. 7b). The two-color anti-counterfeiting strategy leverages the complexity of the internal energy-level structures within CKLC:0.3%Sb^{3+}/25%Ho^{3+}. The obtained materials respond to excitation light of varying energies by emitting at distinct wavelengths, thereby realizing high-level anti-counterfeiting through this dynamic color-changing characteristic. Specifically, the "SWU" mold with CKLC:0.3%Sb^{3+}/25%Ho^{3+} appears white under natural light and ultraviolet light, and red under blue light (450 nm). In addition, use of optical encryption technology has attracted wide attention as a new encryption method in recent years. Therefore, we coated digital molds with CKLC:0.3%Sb^{3+}, CKLC:0.3%Sb^{3+}/25%Ho^{3+} and CKLC:10%Er^{3+}/35%Yb^{3+}, respectively, achieving a consistent appearance for each doped material. Under natural light as well as UV light we can only see the false information "8888" and "6398". Only when excited at 450 and 980 nm is the genuine information of "1750" and "711" shown, thus achieving the function of information encryption (Fig. 7c). Furthermore, we measured the PL spectra of the as-synthesized samples on the day of preparation and again after 20 days (Fig. S8). The emission intensity of the samples after 20 days decreased to 0.87 (CKLC), 0.80 (CKLC:0.3%Sb^{3+}), 0.71 (CKLC:10%Er^{3+}/35%Yb^{3+}), and 0.87 (CKLC:0.3%Sb^{3+}/25% Ho^{3+}) of their initial values, respectively (Fig. S9). These results indicate that CKLC and its doped derivatives exhibit good stability, which is beneficial for the material's application in the field of anti-counterfeiting and information encryption.

4. Conclusion

In conclusion, we have synthesized a novel DP CKLC with weak cyan emission due to STEs. Sb^{3+} doping greatly enhances the intensity of STE emission and increases the PLQY from 2% to 68%. In the Sb^{3+}/Ho^{3+} co-doped system, red emission originating from the f–f transition of Ho^{3+} was also observed. It was demonstrated by steady-state and transient PL spectra that an ET channel exists between STEs and Ho^{3+}. The ET from dopant STEs to Ho^{3+} was more efficient than that from host STEs to Ho^{3+}, overcoming the weak emission due to the weak absorption cross-section of the f–f transition of Ho^{3+}. Moreover, the emission color of the co-doped samples changed from cyan to white and finally to red as the Ho^{3+} concentration increased. In addition to indirect excitation, Ho^{3+} can be directly excited, and thus there is excitation wavelength-dependent luminescence in the co-doped sample. To obtain more luminescence possibilities, we also introduced Er^{3+}/Yb^{3+} and demonstrated that its luminescence mechanism features a three-photon absorption process. Finally, the ion-doped samples were used together to design an anti-counterfeit label and information encryption strategy.

Conflicts of interest

There are no conflicts of interest to declare.

Data availability

All relevant data are within the article and its supplementary information (SI). Supplementary information is available. See DOI: https://doi.org/10.1039/d5dt02031j.

Acknowledgements

This project was financially sponsored by the National Natural Science Foundation of China (NSFC52172154).

References

1 B. Yoon, J. Lee, I. S. Park, S. Jeon, J. Lee and J.-M. Kim, Recent functional material based approaches to prevent and detect counterfeiting, *J. Mater. Chem. C*, 2013, **1**, 2388–2403.
2 Y. Sun, X. Le, S. Zhou and T. Chen, Recent Progress in Smart Polymeric Gel-Based Information Storage for Anti-Counterfeiting, *Adv. Mater.*, 2022, **34**, 2201262.
3 Y. Shi, S. Zhao, Y. Zhou and Z. Zang, Variable halide perovskites: diversification of anti-counterfeiting applications, *Mater. Chem. Front.*, 2023, **7**, 6085–6106.
4 P. Kumar, S. Singh and B. K. Gupta, Future prospects of luminescent nanomaterial based security inks: from synthesis to anti-counterfeiting applications, *Nanoscale*, 2016, **8**, 14297–14340.
5 A. F. Smith and S. E. Skrabalak, Metal nanomaterials for optical anti-counterfeit labels, *J. Mater. Chem. C*, 2017, **5**, 3207–3215.

6 L. Shang, W. Zhang, K. Xu and Y. Zhao, Bio-inspired intelligent structural color materials, *Mater. Horiz.*, 2019, **5**, 945–958.
7 X. Yu, H. Zhang and J. Yu, Luminescence anti-counterfeiting: From elementary to advanced, *Aggregate*, 2021, **2**, 20–34.
8 Y. Xie, Y. Song, G. Sun, P. Hu, A. Bednarkiewicz and L. Sun, Lanthanide-doped heterostructured nanocomposites toward advanced optical anti-counterfeiting and information storage, *Light: Sci. Appl.*, 2022, **11**, 150.
9 M. Tan, F. Li, X. Wang, R. Fan and G. Chen, Temporal Multilevel Luminescence Anticounterfeiting through Scattering Media, *ACS Nano*, 2020, **14**, 6532–6538.
10 Y.-J. Ma, Z. Qi, G. Xiao, X. Fang and D. Yan, Metal-Halide Coordination Polymers with Excitation Wavelength- and Time-Dependent Ultralong Room-Temperature Phosphorescence, *Inorg. Chem.*, 2022, **61**, 16477–16483.
11 S.-Y. Liang, Y.-F. Liu, S.-Y. Wang, Z.-K. Ji, H. Xia, B.-F. Bai and H.-B. Sun, High-Resolution Patterning of 2D Perovskite Films through Femtosecond Laser Direct Writing, *Adv. Funct. Mater.*, 2022, **32**, 0224957.
12 X. Huang, Q. Guo, D. Yang, X. Xiao, X. Liu, Z. Xia, F. Fan, J. Qiu and G. Dong, Reversible 3D laser printing of perovskite quantum dots inside a transparent medium, *Nat. Photonics*, 2020, **14**, 82–88.
13 X. Le, H. Shang, S. Wu, J. Zhang, M. Liu, Y. Zheng and T. Chen, Heterogeneous Fluorescent Organohydrogel Enables Dynamic Anti-Counterfeiting, *Adv. Funct. Mater.*, 2021, **31**, 2108365.
14 C. Yang, L. Gu, C. Ma, M. Gu, X. Xie, H. Shi, H. Ma, W. Yao, Z. An and W. Huang, Controllable co-assembly of organic micro/nano heterostructures from fluorescent and phosphorescent molecules for dual anti-counterfeiting, *Mater. Horiz.*, 2019, **6**, 984–989.
15 Y. Wu, J. Xu, X. Qin, J. Xu and X. Liu, Dynamic upconversion multicolour editing enabled by molecule-assisted opto-electrochemical modulation, *Nat. Commun.*, 2021, **12**, 2022.
16 L. Xu, J. Chen, J. Song, J. Li, J. Xue, Y. Dong, B. Cai, Q. Shan, B. Han and H. Zeng, Double-Protected All-Inorganic Perovskite Nanocrystals by Crystalline Matrix and Silica for Triple-Modal Anti-Counterfeiting Codes, *ACS Appl. Mater. Interfaces*, 2017, **9**, 26556–26564.
17 D. Zhang, W. Zhou, Q. Liu and Z. Xia, $CH_3NH_3PbBr_3$ Perovskite Nanocrystals Encapsulated in Lanthanide Metal-Organic Frameworks as a Photoluminescence Converter for Anti-Counterfeiting, *ACS Appl. Mater. Interfaces*, 2018, **10**, 27875–27884.
18 P. Kumar, T. D. Creason, H. Fattal, M. Sharma, M.-H. Du and B. Saparov, Composition-Dependent Photoluminescence Properties and Anti-Counterfeiting Applications of A_2AgX_3 (A= Rb, Cs; X= Cl, Br, I), *Adv. Funct. Mater.*, 2021, **31**, 2104941.
19 F. Zhang, W. Liang, L. Wang, Z. Ma, X. Ji, M. Wang, Y. Wang, X. Chen, D. Wu, X. Li, Y. Zhang, C. Shan and Z. Shi, Moisture-Induced Reversible Phase Conversion of Cesium Copper Iodine Nanocrystals Enables Advanced Anti-Counterfeiting, *Adv. Funct. Mater.*, 2021, **31**, 2105771.
20 J. Chen, Y. Zeng, R. Sun, W. Zhang, Y. Huang, J. Zheng and Y. Chi, Hydrochromic Perovskite System with Reversible Blue-Green Color for Advanced Anti-Counterfeiting, *Small*, 2023, **19**, 2301010.
21 Y. Pei, D. Tu, C. Li, S. Han, Z. Xie, F. Wen, L. Wang and X. Chen, Boosting Near-Infrared Luminescence of Lanthanide in $Cs_2AgBiCl_6$ Double Perovskites via Breakdown of the Local Site Symmetry, *Angew. Chem., Int. Ed.*, 2022, **61**, e202205276.
22 C. N. Savory, A. Walsh and D. O. Scanlon, Can Pb-Free Halide Double Perovskites Support High-Efficiency Solar Cells?, *ACS Energy Lett.*, 2016, **1**, 949–955.
23 J. Luo, X. Wang, S. Li, J. Liu, Y. Guo, G. Niu, L. Yao, Y. Fu, L. Gao, Q. Dong, C. Zhao, M. Leng, F. Ma, W. Liang, L. Wang, S. Jin, J. Han, L. Zhang, J. Etheridge, J. Wang, Y. Yan, E. H. Sargent and J. Tang, Efficient and stable emission of warm-white light from lead-free halide double perovskites, *Nature*, 2018, **563**, 541–545.
24 Y. Wang, P. Dang, L. Qiu, G. Zhang, D. Liu, Y. Wei, H. Lian, G. Li, Z. Cheng and J. Lin, Multimode Luminescence Tailoring and Improvement of $Cs_2NaHoCl_6$ Cryolite Crystals via Sb^{3+}/Yb^{3+} Alloying for Versatile Photoelectric Applications, *Angew. Chem., Int. Ed.*, 2023, **62**, e202311699.
25 Y. Zhu, G. Pan, J. Zhao, K. Liu, W. Xue, Y. Wang, W. You, H. Gao, W. Xu and Y. Mao, High-Efficiency Dual-Mode Polychromatic Emission of Rare-Earth-Based Double Perovskite with Low Phonon Energy toward High-Level Anti-Counterfeiting and Information Encryption, *Adv. Opt. Mater.*, 2023, **11**, 2202019.
26 X. Liu, X. Xu, B. Li, L. Yang, Q. Li, H. Jiang and D. Xu, Tunable Dual-Emission in Monodispersed Sb^{3+} /Mn^{2+} Codoped $Cs_2NaInCl_6$ Perovskite Nanocrystals through an Energy Transfer Process, *Small*, 2020, **16**, 2002547.
27 R. Zeng, L. Zhang, Y. Xue, B. Ke, Z. Zhao, D. Huang, Q. Wei, W. Zhou and B. Zou, Highly Efficient Blue Emission from Self-Trapped Excitons in Stable Sb^{3+}-Doped $Cs_2NaInCl_6$ Double Perovskites, *J. Phys. Chem. Lett.*, 2020, **11**, 2053–2061.
28 L. Zhou, J.-F. Liao, Z.-G. Huang, J.-H. Wei, X.-D. Wang, W.-G. Li, H.-Y. Chen, D.-B. Kuang and C.-Y. Su, A Highly Red-Emissive Lead-Free Indium-Based Perovskite Single Crystal for Sensitive Water Detection, *Angew. Chem., Int. Ed.*, 2019, **58**, 5277–5281.
29 R. Zhang, Z. Wang, X. Xu, X. Mao, J. Xiong, Y. Yang and K. Han, All-Inorganic Rare-Earth Halide Double Perovskite Single Crystals with Highly Efficient Photoluminescence, *Adv. Opt. Mater.*, 2021, **9**, 2100689.
30 Z. Wang, R. Zhang, X. Mao, D. Zheng, S. Liu, F. Liu, K. Han and B. Yang, Boosting the Self-Trapped Exciton Emission in Cs_2NaYCl_6 Double Perovskite Single Crystals and Nanocrystals, *J. Phys. Chem. Lett.*, 2022, **13**, 8613–8619.
31 B. Chen, Y. Guo, Y. Wang, Z. Liu, Q. Wei, S. Wang, A. L. Rogach, G. Xing, P. Shi and F. Wang, Multiexcitonic Emission in Zero-Dimensional Cs_2ZrCl_6:Sb^{3+} Perovskite Crystals, *J. Am. Chem. Soc.*, 2021, **143**, 17599–17606.

32 W. Huang, H. Peng, Q. Wei, J. Xia, X. He, B. Ke, Y. Tian and B. Zou, Tunable Efficient White Emission in Holmium Doped Double Perovskites Cs_2KInCl_6 via Antimony Sensitization, *Adv. Opt. Mater.*, 2023, **11**, 2203103.

33 S. Bai, H. Liang, C. Li, C. Tang, G. Yang, X. Xu, X. Yang, G. Pan and Y. Zhu, Tunable dual-emission in Sb^{3+}, Mn^{2+} codoped rare-earth based Cs_2NaYCl_6 nanocrystals and its LEDs applications, *Ceram. Int.*, 2023, **49**, 1102–1107.

34 B. Wang, Y. Tang, X. Yang, W. Cai, R. Li, W. Ma, S. Zhao, C. Chen and Z. Zang, Stable yellow light emission from lead-free copper halides single crystals for visible light communication, *Nano Mater. Sci.*, 2023, **5**, 78–85.

35 Y. Liu, R. Yun, H. Yang, W. Sun, Y. Li, H. Lu, L. Zhang and X. Li, Lattice doping of lanthanide ions in Cs_2ZrCl_6 nanocrystals enabling phase transition and tunable photoluminescence, *Mater. Horiz.*, 2024, **11**, 5341–5351.

36 Y. Ning, S. Guan, C. Cheng, B. Zhang, B. Qin and B. Huang, Microfluidic synthesis of monodispersed sharp emitting perovskite $CsPbBr_3$ quantum dots via multidimensional parameterization, *J. Mater. Chem. C*, 2025, **13**, 758–765.

37 X. Li, S. Xu, F. Liu, J. Qu, H. Shao, Z. Wang, Y. Cui, D. Ban and C. Wang, Bi and Sb Codoped $Cs_2Ag_{0.1}Na_{0.9}InCl_6$ Double Perovskite with Excitation-Wavelength-Dependent Dual-Emission for Anti-Counterfeiting Application, *ACS Appl. Mater. Interfaces*, 2021, **13**, 31031–31037.

38 E. W. J. L. Oomen, W. M. A. Smit and G. Blasse, On the luminescence of Sb^{3+} in Cs_2NaMCl_6 (with M=Sc,Y,La): a model system for the study of trivalent s^2 ions, *J. Phys. C: Solid State Phys.*, 1986, **19**, 3263.

39 J. Nie, B. Zhou, S. Fang, H. Zhong, H. Li and Y. Shi, Efficient Multicolor and White Photoluminescence in Erbium- and Holmium-Incorporated $Cs_2NaInCl_6$:Sb^{3+} Double Perovskites, *Chem. Mater.*, 2022, **34**, 6288–6295.

40 Y. Li, H. Du, Y. Ma, M. Liu, J. Zou, S. Wang, J. Yang, S. Hu and J. Lin, Construction of energy transfer channels from $[SbCl_6]^{3-}$ to Ln^{3+} (Ln^{3+} = Ho^{3+}, Er^{3+}) in $Cs_2NaGdCl_6$ for advanced anti-counterfeiting materials, *J. Mater. Chem. C*, 2024, **12**, 12589–12597.

41 N. Singh, V. Singh, S. Watanabe, J. F. D. Chubaci, T. K. G. Rao, H. Gao and P. Mardina, Studies of defects and optical properties of $CaAl_{12}O_{19}$:Ho^{3+} phosphor material, *J. Alloys Compd.*, 2016, **663**, 235–242.

42 B. Dong, C. R. Li and M. K. Lei, Green and red up-conversion emissions of Er^{3+}-Yb^{3+}-codoped Al_2O_3 powders prepared by the nonaqueous sol-gel method, *J. Lumin.*, 2007, **126**, 441–446.

43 G. Y. Chen, Y. Liu, Y. G. Zhang, G. Somesfalean, Z. G. Zhang, Q. Sun and F. P. Wang, Bright white upconversion luminescence in rare-earth-ion-doped Y_2O_3 nanocrystals, *Appl. Phys. Lett.*, 2007, **91**, 133103.

44 Q. Chen, L. Qin, Z. Feng, R. Ge, X. Zhao and H. Xu, Upconversion luminescence of $KGd(MoO_4)_2$:Er^{3+},Yb^{3+} powder prepared by Pechini method, *J. Rare Earths*, 2011, **29**, 843–848.

45 P. Du, Z. Xia and L. Liao, Luminescence properties of $Ca_{0.65}La_{0.35}F_{2.35}$:$Yb^{3+}$, Er^{3+} with enhanced red emission via upconversion, *Mater. Res. Bull.*, 2011, **46**, 543–546.

46 X. Gao, D. Xu, J. Du, Z. Yang and J. Sun, Luminescence properties of Y_2WO_6:Yb^{3+}/Er^{3+} with enhanced red emission via upconversion, *J. Rare Earths*, 2017, **35**, 1065–1070.

47 M. T. Berry and P. S. May, Disputed Mechanism for NIR-to-Red Upconversion Luminescence in $NaYF_4$:Yb^{3+},Er^{3+}, *J. Phys. Chem. A*, 2015, **119**, 9805–9811.